PCCP

PAPER

View Article Online
View Journal | View Issue

Cite this: *Phys. Chem. Chem. Phys.*, 2015, **17**, 30712

Revealing the working mechanism of polymer photodetectors with ultra-high external quantum efficiency†

Lingliang Li,[a] Fujun Zhang,*[a] Wenbin Wang,[a] Yanjun Fang[b] and Jinsong Huang*[b]

Received 17th September 2015,
Accepted 20th October 2015

DOI: 10.1039/c5cp05557a

www.rsc.org/pccp

We report polymer photodetectors (PPDs) with an evident photomultiplication (PM) phenomenon, based on a sandwich structure ITO/PEDOT:PSS/P3HT:$PC_{71}BM$(100:1)/Al. A similar device structure has been reported in our previous work, showing great potential as a new type of high performance PPD. However, we found more interesting new phenomena from these PPDs. Solid evidence is provided to prove the existence of photogenerated electron transport in the almost hole-only active layer under an applied bias. The transport of photogenerated electrons leads to electron accumulation near the Al electrode and the electron redistribution, which strongly affect the EQE spectral shape and the transient response of the PPDs. Our conclusion is further confirmed by confirmatory devices with a structure of Al(1)/P3HT:$PC_{71}BM$(100:1)/Al(2). EQE spectra and transient J_{ph} curves of the confirmatory devices accord well with our speculation. This discovery may provide a new insight to increase the response speed of PM type PPDs by adjusting the photogenerated electron distribution in the active layer. Considering that the PM type PPDs have much higher EQE than the traditional organic photodetectors, the improvement may further extend its potential applications with low cost.

Introduction

Organic photodetectors are receiving ever growing attention due to their ease of fabrication, wide selection of materials and large-area processing capability.[1] There is growing interest in the development of colour selective,[2–4] ultraviolet,[5] near-infrared,[6] and panchromatic[7] organic photodetectors. Most of the organic photodetectors are of photodiode type with photocurrent originating from the collection of photogenerated charge carriers.[8,9] Low background noise and fast response of photodiode type organic photodetectors are beneficial to practical applications such as optical communication, remote control and image sensing.[10–12] The pre-amplifiers are needed to read the weak photocurrent of photodetectors with low external quantum efficiency (EQE) values under weak light conditions,[13] which may bring a new source of noise and make the system more expensive. Therefore, the potential application of photodiode type organic photodetectors may be limited due to the relatively low EQE values (usually lower than 100%). The most important challenge of organic photodetectors is to obtain ultra-high EQE under weak light conditions.[14,15]

The photomultiplication (PM) phenomenon represents a large number of charge carriers flowing across a photodetector per incident photon, resulting in EQE values (*i.e.* photoconductive gain factors or multiplication rates) higher than 100%.[16,17] It is rather difficult to realize the PM phenomenon in organic photodetectors based on the mechanism of photomultiplier tubes or avalanche photodiodes due to the relatively high binding energy of organic semiconductors.[18] However, alternative strategies have been successfully realized for obtaining the PM phenomenon in organic photodetectors: a co-planar structure with or without trap-assisted injection (including photoconductors and phototransistors),[19–21] a sandwich structure with trap-assisted charge carrier tunneling injection,[18] and a sandwich structure with blocking-layer-assisted charge carrier tunneling injection.[22] The mechanism of PM phenomenon in organic photodetectors is that the photogenerated holes or electrons are trapped or blocked in the active layers, while opposite charge carriers continually pass through the active layers and are collected by the corresponding electrode. Chuang *et al.* reported highly sensitive polymer photodetectors (P3HT:$PC_{61}BM$:Ir-125:Q-switch1 = 1:1:0.5:0.5 wt%) with the PM phenomenon, which is attributed to the unbalanced carrier

[a] *Key Laboratory of Luminescence and Optical Information, Ministry of Education, Beijing Jiaotong University, Beijing 100044, People's Republic of China. E-mail: fjzhang@bjtu.edu.cn*

[b] *Department of Mechanical and Materials Engineering and Nebraska Center for Materials and Nanoscience, University of Nebraska–Lincoln, Lincoln, Nebraska 68588-0656, USA. E-mail: jhuang2@unl.edu*

† Electronic supplementary information (ESI) available: Detailed optical field distribution, EQE spectra, transmittance spectra, transient J_{ph} curves and the spectrum of the light source used in this work. See DOI: 10.1039/c5cp05557a

transport in the active layers with dye materials as electron traps.[23] Chen reported organic–inorganic hybrid photodetectors based on composites of P3HT : $PC_{61}BM$: CdTe (1 : 1 : 3.1 wt%) with the PM phenomenon under a low reverse bias of 4.5 V, which is also attributed to the unbalanced carrier transport in the active layers with CdTe nanoparticles as electron traps.[24] Guo reported PM type hybrid photodetectors based on a polymer/inorganic nanocomposite of PVK : ZnO and P3HT : ZnO (both 1 : 3 wt%) as the active layer.[25] The hybrid photodetectors exhibit high EQE values and a rather low dark current under -9 V bias for the absence of a continuous electron transport channel in the active layers and the rather high Schottky barrier for hole injection. Recently, we successfully fabricated PM type polymer photodetectors (PPDs) using P3HT : $PC_{71}BM$ or P3HT : $PC_{61}BM$ (both 100 : 1 wt%) as the active layers sandwiched between ITO and Al electrodes, exhibiting EQE values higher than 16 700% or 37 500%,[26,27] which are among the highest reported values for photodetectors prepared from solely polymer/organic materials. Meanwhile, the detectivity is as high as about 3.5×10^{13} Jones even though our PM type PPDs are without a charge blocking layer or any other optimization. For the active layers with a rather low fullerene derivation content, electron and hole injection barriers are $\sim$1.7 eV and $\sim$0.9 eV from ITO into the lowest unoccupied molecular orbital (LUMO) of P3HT and from Al into the highest occupied molecular orbital (HOMO) of P3HT under reverse bias and dark conditions, resulting in a rather low dark current and high detectivity. The small amount of $PC_{71}BM$ or $PC_{61}BM$ will form nano-size aggregates in the P3HT matrix, which can be considered as bulk electron traps according to the energy level alignment. This speculation can be further confirmed from the research on polymer solar cells, the optimized donor/acceptor doping weight ratio is about 1 : 1 to form a bicontinuous interpenetrating network for efficient charge carrier transport.[28–30] Up to now, the PM type PPDs based on P3HT : PCBM (100 : 1) as the active layer have not been commonly approved although the PPDs exhibit rather high EQE values. Therefore, a more detailed investigation should be carried out to further clarify the key physical issues in PM type PPDs.

Experimental

Preparation of the solutions

P3HT (Product No: LT-S909, purchased from Luminescence Technology Corp.) and $PC_{71}BM$ (Product No: LT-S923, purchased from Luminescence Technology Corp.) were dissolved in 1,2-dichlorobenzene (extra pure, purchased from J&K Scientific Ltd.) to prepare 40 mg ml^{-1} solutions, respectively. Then, the P3HT and $PC_{71}BM$ solutions were blended in a volume ratio of 100 : 1.

Fabrication of the PPDs

ITO glass substrates with a sheet resistance of 15 Ω $square^{-1}$ (purchased from Shenzhen Jinghua Display Co., Ltd.) were precleaned by ultrasonic treatment in detergent, deionised water and ethanol sequentially. Then, all the substrates were dried by nitrogen-gas and treated by UV-ozone for 10 minutes to increase the work function of the ITO substrate. The solution of PEDOT:PSS (Clevios P VP. Al 4083, purchased from Heraeus Precious Metal Gmbh & Co. KG) was spin-coated onto the ITO glass substrates at 5000 rounds per minute (rpm) for 40 s. The PEDOT:PSS coated ITO glass substrates were baked in air at 120 °C. After drying for 10 minutes, the substrates were transferred into a nitrogen-filled glove box. The P3HT:$PC_{71}BM$ blend solution was spin-coated onto the PEDOT:PSS layers at 800 rpm for 30 s to prepare the active layers. The Al electrode of about 100 nm was deposited on the active layers under vacuum (10^{-4} Pa) conditions. The active area of each PPD is about 3.8 mm^2, which is defined by the vertical overlap of the ITO electrode and the Al electrode.

Fabrication of the confirmatory devices

The Al(1) layers of 20 nm thickness were deposited onto the precleaned glass substrates under vacuum (10^{-4} Pa) conditions. The P3HT:$PC_{71}BM$ blend solution was spin-coated onto the Al(1) layers at 800 rpm for 30 s to prepare the active layers. Then, the Al(2) layers of about 100 nm were deposited on the active layers under vacuum (10^{-4} Pa) conditions. The active area is about 2.25 mm^2, which is defined by the vertical overlap of the Al(1) and Al(2) electrodes.

Measurements

Current densities of PPDs and confirmatory devices were measured using the Keithley 2400 Source Meter. The monochromatic light used in all measurements was provided by a 150 W xenon lamp coupled with a monochromator. The light intensity spectrum of monochromatic light was recorded using a Thorlabs S120VC power meter and is shown in Fig. S4, ESI.† The light-on timing and bias-on timing in the transient photocurrent experiment were controlled by electrical shutters and electromagnetic relays, respectively. Absorption and transmittance spectra of films were recorded using a Shimadzu UV-3101 PC spectrophotometer. The active layer thickness of PPDs and confirmatory devices was measured using an Ambios technology XP-2 stylus profilometer. The thickness of the Al(1) electrode was monitored by quartz monitor crystals and checked by the Ambios technology XP-2 stylus profilometer.

Calculation

EQE and responsivity (R) of photodetectors are calculated according to the following equations

$$\mathrm{EQE} = \frac{J_{\mathrm{ph}} h\nu}{I_{\mathrm{in}} e} \quad (1)$$

$$R = \frac{J_{\mathrm{ph}}}{I_{\mathrm{in}}} \quad (2)$$

Here, J_{ph} is the photocurrent density, $h\nu$ is the photon energy, I_{in} is the incident light intensity and e is the absolute value of electron charge.

Based on the assumption that noise-current is dominated by shot noise in the dark current, the corresponding detectivity

(D^*), which describes the signal-to-noise performances of the photodetectors, can be inferred as:[8,31]

$$D^* = \frac{R}{\sqrt{2eJ_d}} \quad (3)$$

Here, J_d is the dark current density.

Results and discussion

In this work, ultrasensitive PPDs with a distinct PM phenomenon were obtained based on P3HT : $PC_{71}BM$ (100 : 1 wt%) as the active layers. A distinct EQE spectral shape dependence on the bias is observed, which may be attributed to the redistribution of photogenerated electrons under different biases. The redistribution of photogenerated electrons in the active layer can be effectively confirmed from the transient J_{ph} curves under different wavelength light illumination and different biases, which may be the main underlying reason for the relatively slow response of PM type PPDs.

The EQE spectra of the PPDs were recorded under different biases, as shown in Fig. 1a. It is apparent that the EQE values of PPDs are much higher than 100% in the wide spectral range from 350 nm to 750 nm. There is a distinct dip at about 520 nm and two peaks at about 400 nm and 625 nm in the EQE spectra of the PPDs. The maximum EQE values of PPDs at 400 nm and 625 nm arrive to about 112 100% and 107 400% under −25 V bias, respectively. The PM phenomenon is attributed to the trap-assisted hole tunneling injection from the Al electrode into the HOMO level of P3HT.[26] For the P3HT:$PC_{71}BM$ blend films with 1 wt% $PC_{71}BM$, $PC_{71}BM$ molecules or aggregates can be considered as electron traps in the P3HT matrix due to the relatively high barrier of about 1.3 eV between the LUMO levels of P3HT (−3.0 eV) and $PC_{71}BM$ (−4.3 eV). The trapped electrons in $PC_{71}BM$ near the Al electrode can induce the interfacial band bending, resulting in the narrower barrier for the stronger hole tunneling injection. To obtain more solid experimental results to reveal the underlying mechanism of PPDs, all PPDs were pretreated by a burn-in treatment under high bias.

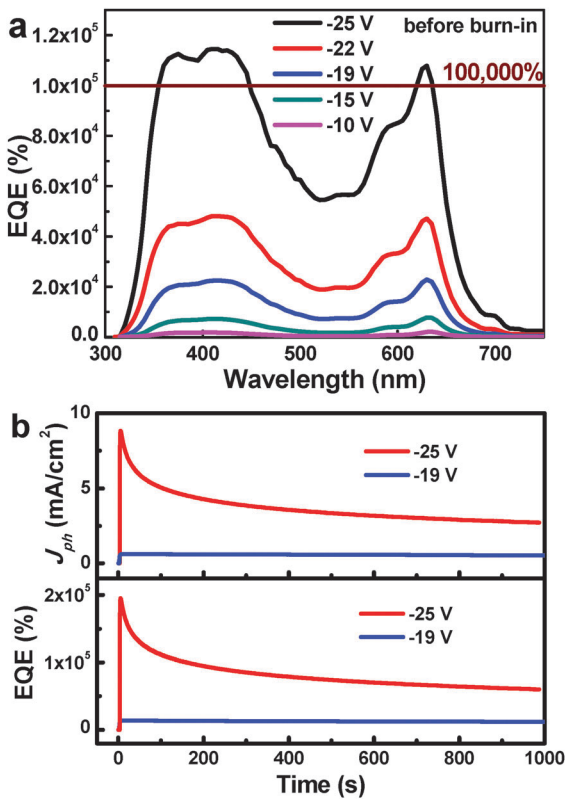

Fig. 1 (a) EQE spectra of PPDs (without burn-in treatment). (b) J_{ph} and EQE value dependence on burn-in time, first treatment: under 400 nm light illumination with 14.05 μW cm^{-2} intensity and −25 V bias for 1000 seconds, second treatment: 400 nm light illumination with 14.05 μW cm^{-2} intensity and −19 V bias for another 1000 seconds.

The EQE value as a function of burn-in time is calculated according to the measured J_{ph} as a function of burn-in time, as shown in Fig. 1b. All PPDs were illuminated under 400 nm light with an intensity of 14.05 μW cm^{-2}, the J_{ph} values of PPDs were measured under −25 V bias for 1000 seconds (red curve in Fig. 1b) and then under −19 V bias for another 1000 second treatment (blue curve in Fig. 1b). It is apparent that the J_{ph} and EQE values of PPDs sharply decreased at the first 1000 s burn-in process under −25 V bias and were almost kept constant during the second 1000 s burn-in treatment, indicating that PPDs have reached a relatively stable state.

The stable PPDs provide a platform to clarify the underlying mechanism of PM type PPDs. In the following, characterization of PPDs is based on the devices that have experienced 2000 s burn-in treatments. The J_d, EQE, R and D^* values of PPDs without or with burn-in treatment are summarized in Table 1. The PPDs with burn-in treatments have a light-to-dark-current ratio (J_l–J_d ratio) of about 77 even under a rather weak incident light intensity of 14.05 μW cm^{-2} at 400 nm.

The EQE spectra of PPDs were recorded under different reverse biases and are shown in Fig. 2a. It is apparent that the EQE values increased along with an increase of the reverse bias, especially in the dip range from 490 nm to 570 nm. The apparent dip range in the EQE spectra of PPDs corresponds well to the strong absorption range of P3HT, as marked in Fig. 2a. To reveal the EQE spectral shape dependence on the reverse bias, all EQE spectra of PPDs under different biases are normalized, as shown in Fig. 2b. It is apparent that the dip of EQE spectra becomes shallower along with the increase of the reverse bias. It is known that the EQE values of PPDs strongly depend on the hole tunneling injection which is determined by

Table 1 Dark current density (J_d), EQE values, responsivity (R) and detectivity (D^*) of PPDs with or without burn-in treatment

	−19 V (W)	−19 V (W/O)	−25 V (W/O)
J_d (mA cm^{-2})	7.5×10^{-3}	1.3×10^{-2}	1.6×10^{-1}
EQE (%)	12 600	21 800	112 100
R (A/W)	40.56	70.26	361.16
D^* (Jones)	2.6×10^{13}	3.5×10^{13}	5.0×10^{13}

The values of EQE, R and D^* were measured under 400 nm light illumination; W: with 2000 s burn-in treatment, W/O: without burn-in treatment.

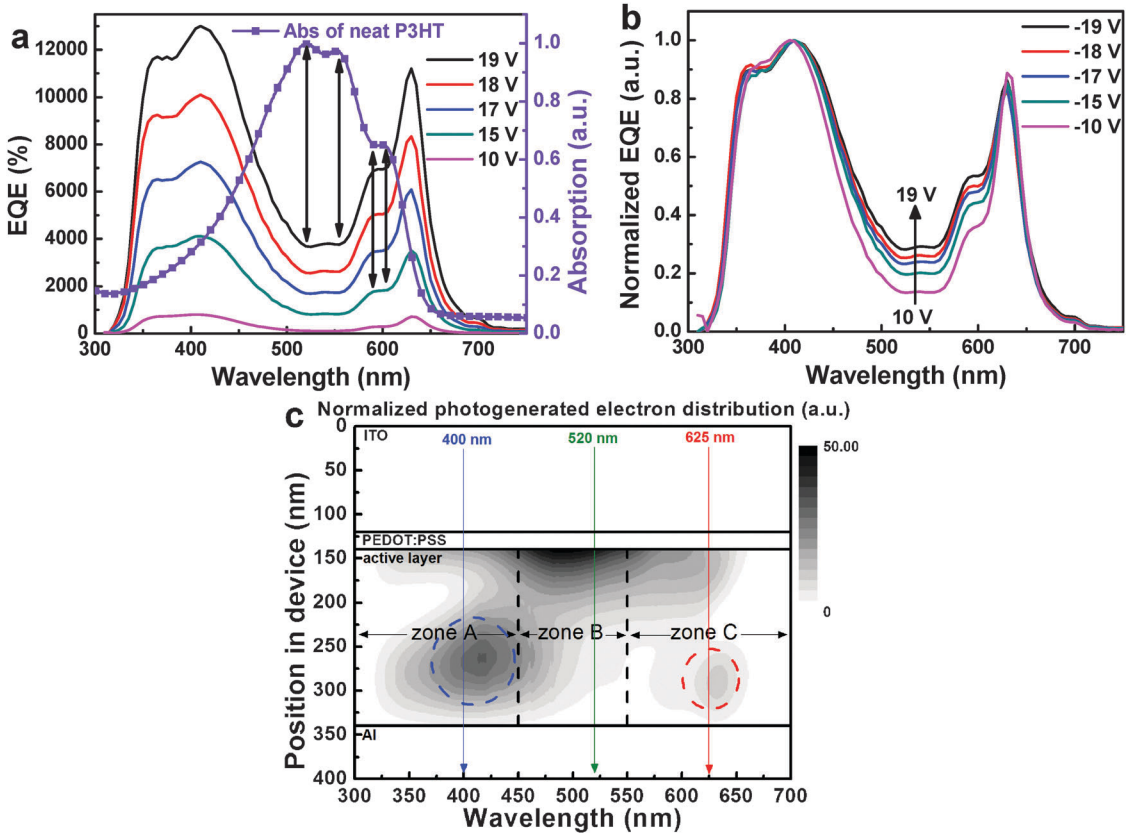

Fig. 2 EQE spectra of PPDs under different reverse biases and the absorption spectrum of neat P3HT films: (a) absolute values and (b) normalized according to the maximum EQE values. (c) The calculated distribution of photogenerated electrons in the active layers (without bias).

the number of trapped electrons in $PC_{71}BM$ near the Al electrode.[26] The variation of EQE spectral shape under different biases indicates that the number of trapped electrons in $PC_{71}BM$ near the Al electrode changed along with the increase of reverse bias due to the redistribution of photogenerated electrons under bias. To confirm this speculation, the optical field distribution in the PPDs was simulated and is shown in Fig. S1, ESI.† An apparent interference phenomenon can be observed due to the superposition between the incident light and the reflected light from the specular Al electrode in the active layers.[32,33]

Assuming that the exciton dissociation coefficient and the absorption coefficient in the bulk films are constant due to good miscibility of P3HT and $PC_{71}BM$,[34,35] the distribution of photogenerated electrons in the active layer (without bias) was calculated according to the optical field distribution and the absorption spectrum of P3HT, as shown in Fig. 2c. The detailed calculation of the distribution of photogenerated electrons in the active layer is described in the ESI.†

For better discussion on the distribution of photogenerated electrons in the active layers, we define three zones A (<450 nm), B (450 to 600 nm) and C (>600 nm), as marked in Fig. 2c. The dark color indicates more photogenerated electrons in the region. It is apparent that much more photogenerated electrons should be trapped in $PC_{71}BM$ near the Al electrode in zone A due to the large dark region (marked by a blue imaginary circle), which can well explain the relatively high EQE values in the wide spectral range from 350 nm to 450 nm. For zone C, there is a relatively small and slight dark region in the range from 600 nm to 650 nm (marked by a red imaginary circle), indicating that fewer electrons are trapped in $PC_{71}BM$ near the Al electrode, which also corresponds well to the narrow peak at 625 nm in the EQE spectra of PPDs. For zones A and C, many photogenerated electrons have already been trapped in $PC_{71}BM$ near the Al electrode, and these electrons play the key role in assisting the hole tunnelling injection from the Al electrode into the HOMO of P3HT. The distribution of photogenerated electrons in zone B is very distinguished from that in zones A and C. Much more photogenerated electrons in zone B are generated near the ITO electrode rather than the Al electrode due to the strong photon harvesting ability of P3HT in this spectral range. Only very few photons can propagate through the active layer and be reflected by the specular Al electrode, resulting in a rather weak interference in this spectral range. As we can envisage, photogenerated electrons near the ITO electrode can be transported toward the Al electrode under the electric field induced by reverse bias, leading to the electron accumulation in $PC_{71}BM$ near the Al electrode. However, this kind of electron accumulation will be hindered by the electrons already trapped near the Al electrode in zones A and C. The redistribution of photogenerated electrons near the Al electrode should determine the hole tunnelling injection due to different degrees of band bending that depend

on the number of trapped electrons in $PC_{71}BM$ near the Al electrode. Therefore, electron accumulation in $PC_{71}BM$ near the Al electrode may be the underlying reason for the more obvious increase of EQE values in zone B along with the increase of reverse bias.

It can be envisaged that electron transport should be rather weak due to the absence of the electron transport channel in the P3HT : $PC_{71}BM$ (100 : 1) films, resulting in a rather slow electron accumulation toward $PC_{71}BM$ near the Al electrode under reverse bias. The rather slow electron accumulation process can be revealed by the transient J_{ph} characteristics of the PPDs. The transient J_{ph} characteristics of all PPDs were measured under different wavelength light illumination and using different measurement methods (turn-on light and then turn-on bias, or turn-on bias and then turn-on light), as shown in Fig. 3a. It is apparent that the saturated J_{ph} values of PPDs under 400 nm and 625 nm light illumination are much larger than that under 520 nm light illumination, which accords well with the EQE spectra of PPDs. For turn-on bias and then turn-on light measurement methods, the rise process of J_{ph} should be co-determined by the photon–electron conversion process and the electron accumulation process in $PC_{71}BM$ near the Al electrode. For turn-on light more than 4 seconds and then the turn-on bias measurement method, the rise process of J_{ph} should be only determined by the electron accumulation process in $PC_{71}BM$ near the Al electrode. The number of photogenerated electrons in $PC_{71}BM$ near the Al electrode has reached a saturation state (dynamic balance) before turn-on bias, because the photon–electron conversion process is ultrafast (in about 100 fs), which has been fully confirmed by the reported investigation of organic solar cells.[36] It can be seen that no matter which measurement method was used, the transient J_{ph} curves are almost coincident under the same wavelength light illumination. It means that the rise process of J_{ph} is mainly determined by the process of electron accumulation in $PC_{71}BM$ near the Al electrode. To further confirm our speculation, the normalized transient J_{ph} curves of PPDs under different wavelength light illumination are shown in Fig. 3b. It is apparent that the J_{ph} of PPDs under 520 nm light illumination will take more time to arrive at its saturation state under the same reverse bias, which should be due to the initial distribution of photogenerated electrons in the active layer and the slow electron accumulation process in $PC_{71}BM$ near the Al electrode under reverse bias. The initial distribution of photogenerated electrons at specific wavelengths (400 nm, 520 nm and 625 nm) is shown in Fig. 3c (as the cross-sections marked in Fig. 2c). It is apparent that more photogenerated electrons are generated near the ITO electrode under 520 nm light illumination due to the high photon harvesting ability of P3HT at this wavelength, those photogenerated electrons are rather difficult to be accumulated in $PC_{71}BM$ near the Al electrode due to the long transport distance. Thus, it will take

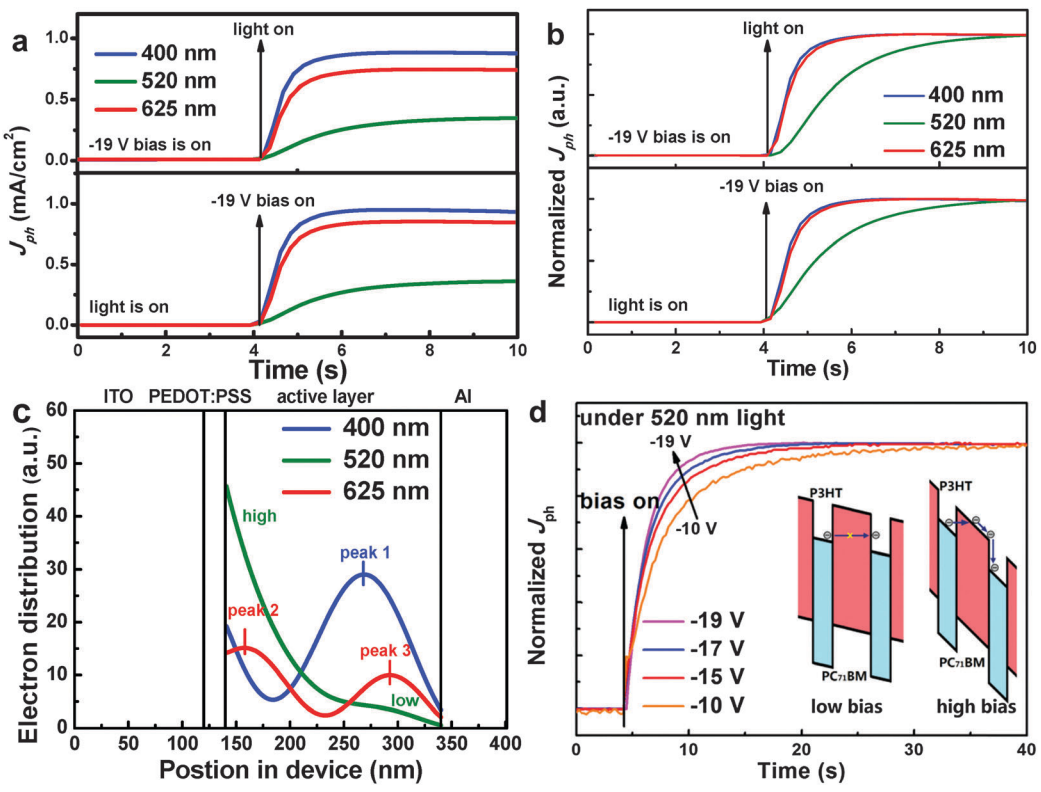

Fig. 3 (a) Transient J_{ph} curves of PPDs measured under 400 nm, 520 nm or 625 nm light illumination and under different operation processes: (i) turn-on −19 V bias and then turn-on the light and (ii) turn-on the light and then turn-on the −19 V bias. (b) Normalized transient J_{ph} curves of PPDs. (c) The normalized calculated electron distribution in PPDs under 400 nm, 520 nm and 625 nm light illumination (under zero bias). (d) The normalized transient J_{ph} curves under different biases for the PPDs under 520 nm light illumination; the insert is a schematic image of electron transport under low and high biases.

more time to accumulate photogenerated electrons in $PC_{71}BM$ near the Al electrode under a reverse bias, which supports well the relatively slow rise process of J_{ph} under 520 nm light illumination. For the PPDs under 400 nm or 625 nm light illumination, many photogenerated electrons have already been trapped in $PC_{71}BM$ far from the ITO electrode according to the peak position in the distribution of photogenerated electrons in the active layer (as marked in Fig. 3c). Those electrons will be easily accumulated in $PC_{71}BM$ near the Al electrode under the reverse bias due to the short transport distance, resulting in a relatively rapid rise process of J_{ph} under 400 nm or 625 nm light illumination.

According to the distribution of photogenerated electrons in the active layers, the effect of electron accumulation process on the J_{ph} rise process should be more obvious under 520 nm light illumination. The transient J_{ph} curves were measured under different reverse biases for the PPDs under 520 nm light illumination, as shown in Fig. 3d. It is apparent that the J_{ph} of PPDs rapidly reaches its saturated state under higher reverse bias due to the faster accumulation of photogenerated electrons in $PC_{71}BM$ near the Al electrode. In fact, photogenerated electrons should overcome the different tunneling barriers to accumulate in $PC_{71}BM$ near the Al electrode under different reverse biases, as shown in the insert of Fig. 3d. Under relatively low reverse bias, photogenerated electrons are difficult to be directly transferred from one trap (small $PC_{71}BM$ aggregation) to another trap (small $PC_{71}BM$ aggregation) by tunneling the rectangular barrier formed by P3HT. Under relatively high reverse bias, photogenerated electrons can be more easily transported from one trap to another trap by tunneling a triangular barrier formed by P3HT due to the more tilted energy levels of P3HT. Therefore, the slow J_{ph} rise process is mainly determined by the slow accumulation process of photogenerated electrons in $PC_{71}BM$ near the Al electrode under different biases.

To further confirm our understanding on the effects of the initial distribution and the redistribution of photogenerated electrons on the performance of PPDs, confirmatory devices with a structure of Al(1)/active layer/Al(2) were fabricated on glass substrates. The P3HT : $PC_{71}BM$ (100 : 1 wt%) blend films were used as the active layers for the confirmatory device. The thickness of the Al(1) layer is about 20 nm to guarantee the functions as both the electrode and the incident light window. We define Al(1) as the anode and Al(2) as the cathode to accurately describe the direction of the applied field. For the confirmatory devices, the hole injection barrier from Al into the HOMO level of P3HT should be the same under forward or reverse bias. Therefore, the EQE values for the PM type PPDs under forward or reverse bias should be only determined by the number of trapped electrons in $PC_{71}BM$ near the Al(1) or Al(2) electrode. The EQE spectra of confirmatory devices were recorded under different reverse biases, as shown in Fig. S2a, ESI.† The EQE spectral shapes of confirmatory devices under different reverse biases are very similar to those of PPDs, however the EQE values are much lower than those of PPDs under the same reverse bias due to the relatively low light transmittance of the Al(1) layer (Fig. S2b, ESI†). The EQE spectra of confirmatory devices recorded under different forward biases are shown in Fig. 4a. No obvious dips can be observed from the EQE spectra of confirmatory devices under forward bias. The EQE values of the confirmatory devices are much higher than 100% under reverse or forward bias. Meanwhile, the confirmatory devices exhibit significantly different EQE spectral shapes under forward or reverse bias, which should be attributed to the different distribution of photogenerated electrons near Al(1) or Al(2) under forward or reverse bias. Here, we focus on the confirmatory devices' EQE spectral dependence on the forward bias to further investigate the effects of the initial distribution and the redistribution of photogenerated electrons on the EQE spectral shape and the J_{ph} rise process of PM type PPDs.

Under forward bias, holes will be injected from the Al(1) electrode assisted by trapped electrons in $PC_{71}BM$ near the Al(1) electrode. Therefore, the EQE spectral shape of confirmatory devices is determined by the electron distribution near the Al(1) electrode under forward bias. The initial distribution of photogenerated electrons in the active layer of confirmatory devices (without bias) is calculated and shown in Fig. 4b. It is apparent that most of the photogenerated electrons are directly trapped in $PC_{71}BM$ near the Al(1) electrode once they are generated, and the trapped electrons in $PC_{71}BM$ near Al(2) can be negligible in

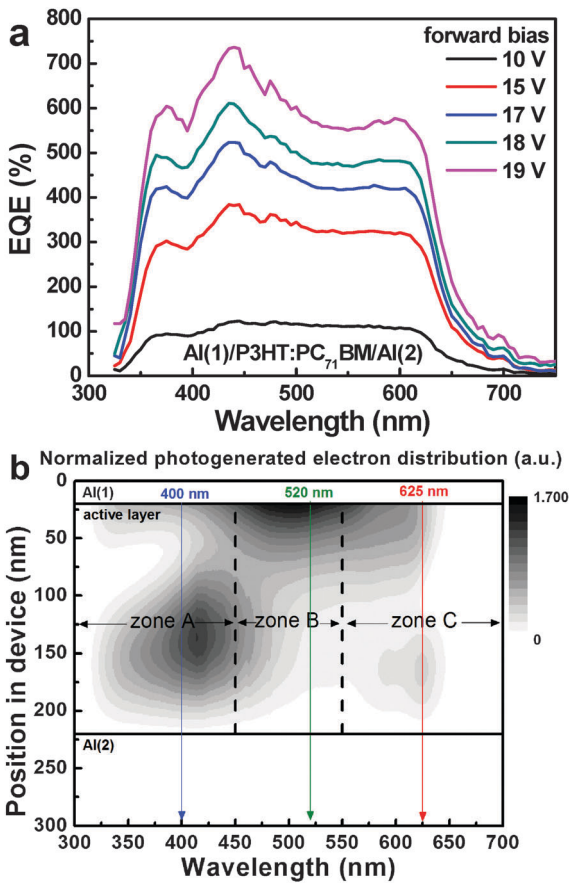

Fig. 4 (a) EQE spectra of confirmatory devices under different forward biases and (b) the calculated distribution of photogenerated electrons in the active layer of confirmatory devices (without bias).

zone B. However, many photogenerated electrons are trapped in $PC_{71}BM$ near the Al(2) electrode in zones A and C. It is known that the photogenerated electrons in the active layer will be transported toward the Al(1) or Al(2) electrode under forward or reverse bias, resulting in different electron redistributions in the active layer, especially in $PC_{71}BM$ near the electrode. Interestingly, EQE values in zone B are not higher than those in zones A and C under forward bias, although most of the electrons are generated near the Al(1) electrode in zone B. It is because the photogenerated electrons in zone B are so near the Al(1) electrode that they can be very easily collected by the Al(1) electrode under forward bias. The photogenerated electrons collected by the Al(1) electrode will not contribute to the EQE of confirmatory devices. Moreover, the relative EQE peaks in zones A and C become more obvious along with the increase of forward bias due to the electron transport toward $PC_{71}BM$ near the Al(1) electrode in zones A and C. The redistribution of electrons in $PC_{71}BM$ near the electrode strongly influences the hole tunneling injection from the corresponding electrode.

To further confirm the effects of distribution and accumulation of photogenerated electrons on the J_{ph} rise process of the confirmatory devices, the transient J_{ph} curves of confirmatory devices were measured under different wavelengths and bias conditions as shown in Fig. S3, ESI.† The normalized transient J_{ph} curves of confirmatory devices are shown in Fig. 5a. It is apparent that the J_{ph} of confirmatory devices under 520 nm light illumination exhibits the fastest rise process under forward bias and the slowest rise process under reverse bias. The different J_{ph} rise processes can be explained well by the redistribution of photogenerated electrons in the active layer induced by an electron accumulation process under bias. The initial distribution of photogenerated electrons under different wavelength light illumination was calculated according to the optical field distribution, as shown in Fig. 5b. It is apparent that most of the electrons generated from 520 nm light illumination should be trapped in $PC_{71}BM$ near the Al(1) electrode. Therefore, these photogenerated electrons will take different times to be accumulated in $PC_{71}BM$ near Al(1) or Al(2) under forward or reverse bias, resulting in distinguished J_{ph} rise processes, respectively. When the confirmatory devices were illuminated at 400 nm or 625 nm light, the J_{ph} rise processes under forward or revere bias are relatively similar due to the relatively analogous distribution of photogenerated electrons and the electron accumulation process.

In order to better understand the electron transport in the active layers of PM type PPDs, schematic diagrams of energy level structure for PPDs under reverse bias and different conditions are shown in Fig. 6. When the PPDs are kept in the dark, holes can hardly be tunnel injected from the Al electrode to the HOMO of P3HT due to the relatively high triangular barrier, as marked in Fig. 6a. When the incident light is just turned on, most of the photogenerated electrons are generated near the ITO side and then trapped in $PC_{71}BM$ near the ITO side, as shown in Fig. 6b. This initial electron distribution can be effectively demonstrated in Fig. 2c and 3c. When most of the photogenerated electrons are accumulated near the ITO side, the interfacial band bending near the Al electrode cannot be

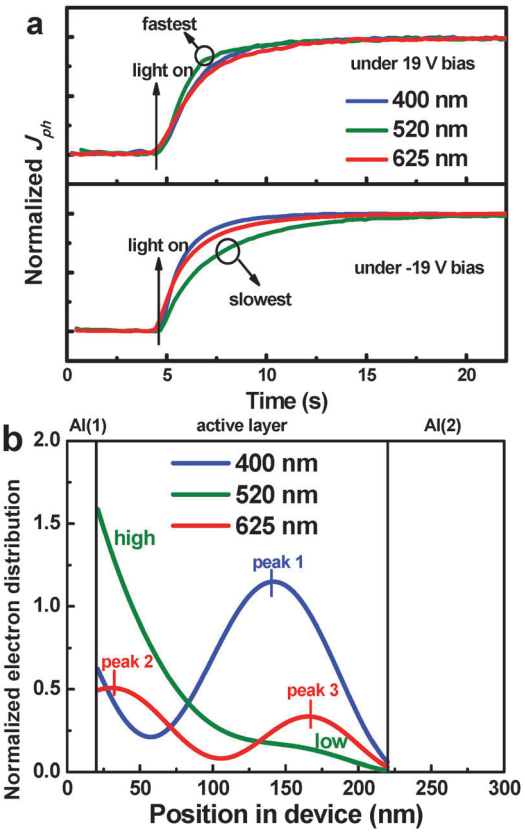

Fig. 5 (a) Normalized transient J_{ph} of the confirmatory devices under 400 nm, 520 nm or 625 nm light illumination and 19 V or −19 V bias. (b) The initial electron distribution in the confirmatory devices under 400 nm, 520 nm and 625 nm light illumination (without bias).

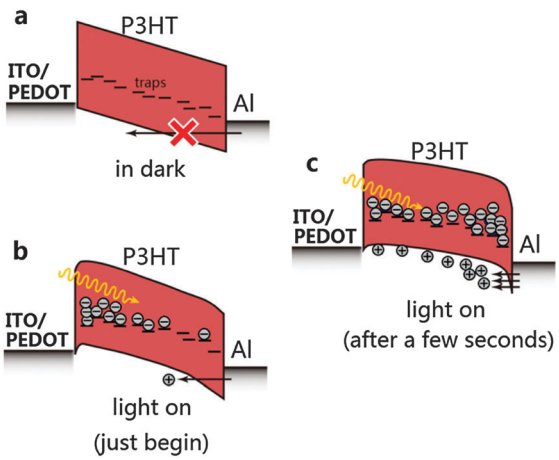

Fig. 6 Schematic diagrams of energy level structure for PPDs under reverse bias and different conditions. (a) Dark conditions, (b) light illumination just begins, and (c) under light illumination for a few seconds.

induced for efficient hole tunneling injection. As we can envisage, the photogenerated electrons will be transported from the ITO side to the Al side under reverse bias. There are two kinds of possibilities for the photogenerated electrons arriving near the Al electrode under reverse bias, one is trapped by $PC_{71}BM$ near the

Al electrode, and the other is collected by the Al electrode. The photogenerated electrons collected by the Al electrode have no function on the trap-assisted hole tunneling injection. Only the trapped electrons in $PC_{71}BM$ near the Al electrode can result in interfacial band bending, which is beneficial to hole tunneling injection from the Al electrode into the HOMO of P3HT. After a few seconds of illumination, the number of trapped electrons in $PC_{71}BM$ near the Al electrode is greatly increased, resulting in a rather narrow hole tunneling injection barrier and enhanced hole tunneling injection, as shown in Fig. 6c. According to the energy levels of used materials, holes are easily injected into the HOMO level of P3HT due to the relatively small 0.9 eV injection barrier and hardly injected into the HOMO level of $PC_{71}BM$ due to the relatively large 1.7 eV interfacial barrier. If the injected holes prefer to recombine with trapped electrons in $PC_{71}BM$, the trap-assisted hole tunneling injection will be decreased resulting in the disappearance of the PM phenomenon. Therefore, the recombination between injected holes and trapped electrons in $PC_{71}BM$ should be very limited due to the rather low $PC_{71}BM$ content in the active layers. The distribution, transport and accumulation of photogenerated electrons in the active layers co-determine the EQE spectral shape and response speed under different wavelength light illumination or applied reverse bias. Based on the above discussion and a recently published paper,[37] the EQE values of our reported PM type PPDs are determined by hole tunneling injection from the Al electrode into the HOMO of P3HT and hole transport along the channels formed by P3HT. The EQE of PM type PPDs was markedly increased by adjusting the P3HT molecular arrangement from "edge-on" to "face-on" models which was realized by controlling the self-assembly time of P3HT:$PC_{71}BM$ active layers before annealing treatment. According to this work and our previously published papers in this year,[26,27,37] the working mechanism of these PM type PPDs should be clearly revealed as follows: (i) photon harvesting by P3HT; (ii) rather small part exciton (close to $PC_{71}BM$) dissociated into charge carriers, with electrons trapped in $PC_{71}BM$ and holes transported along P3HT channels; (iii) electrons accumulated in $PC_{71}BM$ near the Al electrode, resulting in interfacial band bending for better hole tunneling injection; (iv) the injected holes are transported in active layers under the reverse bias; and (v) the injected holes are collected by the ITO electrode. As long as the photogenerated electrons can be trapped in $PC_{71}BM$ near the Al electrode, holes can be continuously injected from the external circuit and transported to the ITO electrode. This is why the EQE of PM type PPDs can be much larger than unit, which provides a great potential application because a pre-amplifier circuit is not necessary for PM type PPDs. It is kept in mind that the response speed of PM type PPDs should be further increased even up to a millisecond scale for satisfying specific needs. Very recently, we have successfully reported the highly sensitive PM type PPDs with a broad spectral response range from the UV to near infrared region.[38] The spectral response range of the PPDs can be extended to the near infrared region by doping a narrow band gap polymer PTB7-Th into P3HT:$PC_{71}BM$ as the active layer. The highest EQE values of PPDs with P3HT : PTB7-Th : $PC_{71}BM$ (50 : 50 : 1) as the active layers are around 38 000% in the spectral range from 625 nm to 750 nm under −25 V bias.[38] It means that our reported PM type PPDs may provide a new platform to obtain broad or adjusted spectral response range PM type polymer photodetectors.

Conclusions

In summary, ultrasensitive PPDs with a distinct PM phenomenon were obtained based on P3HT : $PC_{71}BM$ (100 : 1 wt%) as the active layers. The stable champion EQE value of PPDs was ~12 600% under −19 V bias for the devices with 2000 s burn-in treatment. The PM phenomenon is attributed to the enhanced hole tunneling injection assisted by photogenerated electrons trapped in $PC_{71}BM$ near the Al electrode. The EQE spectral shape and the response speed of PPDs strongly depend on the bias, which can be well explained by the initial distribution of photogenerated electrons in the active layer and the redistribution of photogenerated electrons under different biases. This speculation is well demonstrated by the transient J_{ph} characteristics and EQE spectra of PPDs and confirmatory devices under forward and reverse biases. This discovery may provide a new insight to increase the response speed of PM type PPDs by adjusting the photogenerated electron distribution in the active layer. Considering that PM type PPDs have much higher EQE than the traditional organic photodetectors, the improvement may further extend its potential applications with low cost because a pre-amplifier circuit is not necessary for PM type PPDs.

Acknowledgements

This work was supported by Fundamental Research Funds for the Central Universities (2015YJS176), National Natural Science Foundation of China (61377029), and Beijing Natural Science Foundation (2122050). J. Huang thanks the support from National Science Foundation under award CMM-1265834. Zhang also thanks the support from the one hundred talents project of Beijing Jiaotong University.

Notes and references

1 H. Dong, H. Zhu, Q. Meng, X. Gong and W. Hu, *Chem. Soc. Rev.*, 2012, **41**, 1754–1808.
2 A. Armin, R. D. Jansen-van Vuuren, N. Kopidakis, P. L. Burn and P. Meredith, *Nat. Commun.*, 2015, **6**, 6343.
3 R. D. Jansen-van Vuuren, A. Pivrikas, A. K. Pandey and P. L. Burn, *J. Mater. Chem. C*, 2013, **1**, 3532–3543.
4 K. H. Lee, D. S. Leem, J. S. Castrucci, K. B. Park, X. Bulliard, K. S. Kim, Y. W. Jin, S. Lee, T. P. Bender and S. Y. Park, *ACS Appl. Mater. Interfaces*, 2013, **5**, 13089–13095.
5 H. Lee, S. Nam, H. Kwon, S. Lee, J. Kim, W. Lee, C. Lee, J. Jeong, H. Kim, T. J. Shin and Y. Kim, *J. Mater. Chem. C*, 2015, **3**, 1513–1520.

6 E. Saracco, B. Bouthinon, J. M. Verilhac, C. Celle, N. Chevalier, D. Mariolle, O. Dhez and J. P. Simonato, *Adv. Mater.*, 2013, **25**, 6534–6538.
7 J. Qi, L. Ni, D. Z. Yang, X. K. Zhou, W. Q. Qiao, M. Li, D. G. Ma and Z. Y. Wang, *J. Mater. Chem. C*, 2014, **2**, 2431–2438.
8 X. Gong, M. Tong, Y. Xia, W. Cai, J. S. Moon, Y. Cao, G. Yu, C.-L. Shieh, B. Nilsson and A. J. Heeger, *Science*, 2009, **325**, 1665–1667.
9 D. Baierl, L. Pancheri, M. Schmidt, D. Stoppa, G.-F. Dalla Betta, G. Scarpa and P. Lugli, *Nat. Commun.*, 2012, **3**, 1175.
10 B. Arredondo, B. Romero, J. Pena, A. Fernández-Pacheco, E. Alonso, R. Vergaz and C. de Dios, *Sensors*, 2013, **13**, 12266–12276.
11 Z. Su, F. Hou, X. Wang, Y. Gao, F. Jin, G. Zhang, Y. Li, L. Zhang, B. Chu and W. Li, *ACS Appl. Mater. Interfaces*, 2015, **7**, 2529–2534.
12 T. Rauch, M. Boberl, S. F. Tedde, J. Furst, M. V. Kovalenko, G. N. Hesser, U. Lemmer, W. Heiss and O. Hayden, *Nat. Photonics*, 2009, **3**, 332–336.
13 H. Park, Y.-H. Kuo, A. W. Fang, R. Jones, O. Cohen, M. J. Paniccia and J. E. Bowers, *Opt. Express*, 2007, **15**, 13539–13546.
14 T. Zhai, L. Li, Y. Ma, M. Liao, X. Wang, X. Fang, J. Yao, Y. Bando and D. Golberg, *Chem. Soc. Rev.*, 2011, **40**, 2986–3004.
15 T. Kyu An, C. Eon Park and D. Sung Chung, *Appl. Phys. Lett.*, 2013, **102**, 193306.
16 R. Dong, C. Bi, Q. Dong, F. Guo, Y. Yuan, Y. Fang, Z. Xiao and J. Huang, *Adv. Opt. Mater.*, 2014, **2**, 549–554.
17 R. Saran, V. Stolojan and R. J. Curry, *Sci. Rep.*, 2014, **4**, 5041.
18 S. H. Wu, W. L. Li, B. Chu, Z. S. Su, F. Zhang and C. S. Lee, *Appl. Phys. Lett.*, 2011, **99**, 023305.
19 B. T. Lim, I. Kang, C. M. Kim, S. Y. Kim, S.-K. Kwon, Y.-H. Kim and D. S. Chung, *Org. Electron.*, 2014, **15**, 1856–1861.
20 Z. W. Jin and J. Z. Wang, *Sci. Rep.*, 2014, **4**, 5331.
21 H. H. Xu, J. Li, B. H. K. Leung, C. C. Y. Poon, B. S. Ong, Y. T. Zhang and N. Zhao, *Nanoscale*, 2013, **5**, 11850–11855.
22 W. T. Hammond, J. P. Mudrick and J. Xue, *J. Appl. Phys.*, 2014, **116**, 214501.
23 S.-T. Chuang, S.-C. Chien and F.-C. Chen, *Appl. Phys. Lett.*, 2012, **100**, 013309.
24 H. Y. Chen, M. K. F. Lo, G. W. Yang, H. G. Monbouquette and Y. Yang, *Nat. Nanotechnol.*, 2008, **3**, 543–547.
25 F. W. Guo, B. Yang, Y. B. Yuan, Z. G. Xiao, Q. F. Dong, Y. Bi and J. S. Huang, *Nat. Nanotechnol.*, 2012, **7**, 798–802.
26 L. L. Li, F. J. Zhang, J. Wang, Q. S. An, Q. Q. Sun, W. B. Wang, J. Zhang and F. Teng, *Sci. Rep.*, 2015, **5**, 9181.
27 L. L. Li, F. J. Zhang, W. B. Wang, Q. S. An, J. Wang, Q. Q. Sun and M. Zhang, *ACS Appl. Mater. Interfaces*, 2015, **7**, 5890–5897.
28 Q. S. An, F. J. Zhang, L. L. Li, J. Wang, Q. Q. Sun, J. Zhang, W. H. Tang and Z. B. Deng, *ACS Appl. Mater. Interfaces*, 2015, **7**, 3691–3698.
29 Q. S. An, F. J. Zhang, L. L. Li, J. Wang, J. Zhang, L. Zhou and W. H. Tang, *ACS Appl. Mater. Interfaces*, 2014, **6**, 6537–6544.
30 Q. S. An, F. J. Zhang, J. Zhang, W. H. Tang, Z. Wang, L. L. Li, Z. Xu, F. Teng and Y. S. Wang, *Sol. Energy Mater. Sol. Cells*, 2013, **118**, 30–35.
31 G. Konstantatos and E. H. Sargent, *Nat. Nanotechnol.*, 2010, **5**, 391–400.
32 L. A. A. Pettersson, L. S. Roman and O. Inganäs, *J. Appl. Phys.*, 1999, **86**, 487–496.
33 W. Li, D. Li, G. Dong, L. Duan and L. Wang, *Org. Electron.*, 2014, **15**, 3231–3236.
34 B. A. Collins, J. R. Tumbleston and H. Ade, *J. Phys. Chem. Lett.*, 2011, **2**, 3135–3145.
35 N. D. Treat, M. A. Brady, G. Smith, M. F. Toney, E. J. Kramer, C. J. Hawker and M. L. Chabinyc, *Adv. Energy Mater.*, 2011, **1**, 82–89.
36 C. J. Brabec, N. S. Sariciftci and J. C. Hummelen, *Adv. Funct. Mater.*, 2001, **11**, 15–26.
37 W. B. Wang, F. J. Zhang, L. L. Li, M. L. Gao and B. Hu, *ACS Appl. Mater. Interfaces*, 2015, **7**, 22660–22668.
38 W. B. Wang, F. J. Zhang, L. L. Li, M. Zhang, Q. S. An, J. Wang and Q. Q. Sun, *J. Mater. Chem. C*, 2015, **3**, 7386–7393.

